Supporting Information

Axmacher et al. 10.1073/pnas.0911531107

SI Methods

Subjects. Fourteen patients with pharmacoresistant temporal lobe epilepsy (3 women; mean age ± SD: 38.3 ± 11.8 years) participated in the study. In 11 patients, unilateral hippocampal sclerosis was confirmed histologically. In the others, one had a unilateral isolated amygdala lesion, two had no apparent MRI lesions, and two had unilaterally accentuated limbic pathologies. Recordings were performed from 2004 to 2007 at the Department of Epileptology, University of Bonn, Germany. Thirteen patients had bilateral hippocampal depth electrodes, and only electrode sites contralateral to the epileptogenic zone were considered. One patient had a single electrode in the right hippocampus and an extrahippocampal (temporo-occipital) seizure onset zone. No seizure occurred within 24 h before the experiment. The study was approved by the local medical ethics committee, and all patients gave written informed consent.

Depth Electrodes. Multicontact depth electrodes were inserted for diagnostic purposes using a computed tomography-based stereotactic insertion technique (1). Each electrode (AD-Tech) had 10 platinum-iridium contacts, a diameter of 1.3 mm, and an interelectrode spacing of 4.5 mm. The location of electrode contacts was ascertained by MRI in each patient; Montreal Neurological Institute (MNI) coordinates from the hippocampal contact selected for analysis are given in Table S1. On average, patients had 5.4 ± 1.9 hippocampal contacts (mean ± SD).

Experimental Paradigm. Each picture was presented using ERTS software (BeriSoft). Faces were shown in the center of a computer screen (0.5 s) with a randomized interstimulus interval with a mean of 1.5 s and a range of 1.3–1.7 s ("encoding" phase). Afterward, patients had to maintain the faces in WM for 3 s ("maintenance" phase). Subsequently, patients were presented a probe and had to decide whether it matched one of the presented faces or not. Faces were only used once and were not reused in other trials. Patients indicated their decision by pressing one of two buttons of a computer mouse in their dominant hand. A total of 306 faces were presented to each patient over 108 trials; the overall duration of the experiment was about 20 min. During the experiment, we recorded the continuous EEG from the depth electrodes as well as from bilateral mastoid electrodes.

Analyses. Depth EEG was referenced to linked mastoids, recorded at a sampling rate of 1000 Hz, and band-pass filtered [0.01 Hz (6dB/octave) to 300 Hz (12dB/octave)]. EEG trials were visually inspected for artifacts (e.g., epileptiform spikes), and trials containing artifacts were excluded from analysis. From the contralateral (nonfocal) electrode in each patient, we selected the hippocampal contact with the maximal slope of the DC potential, as this measure likely corresponds to working memory maintenance (2).

EEG trials were subjected to continuous wavelet transforms between 1 Hz and 200 Hz (1-Hz steps) by Morlet wavelets of five-cycle length, resulting in filtered signals $w_{j,k}$, with j indicating the time point within a trial and k the trial number (3). To avoid edge effects, the trials entering the wavelet transform were segmented from –2 s to 5.5 s with respect to presentation of the last stimulus of the series. We selected baseline periods before presentation of this last stimulus to avoid baseline periods including stimulus-related activity. Afterward, 2-s long intervals before and after the 3.5-s maintenance period (including the presentation time of the last stimulus in each trial) were discarded.

List of consecutive analysis steps:

- continuous wavelet transform (1–200 Hz; 1-Hz steps);
- extraction of lower-frequency (1–14 Hz) phases ψ_{LF} and high-frequency (14–200 Hz) amplitudes A_{HF} for each time point;
- construction of the complex signal $z = A_{HF}\, e^{i\psi}{}_{LF}$ and estimation of single-trial modulation phase $\varphi_k(\bar{z}_k)$ for each trial;
- modulation phase $\varphi(\bar{z})$: average single-trial modulation phase across all trials and conditions;
- modulation variance υ: circular variance of the distribution of single-trial modulation phases across trials;
- shift of the lower-frequency signal w_{LF} with $-\varphi(\bar{z})$ yielding $w_{LF}{}^{S}$;
- modulation strength μ: Fisher-z-transformed Pearson's correlation between the real part of the lower-frequency oscillation $Re(w_{LF}{}^{S})$ and the high-frequency amplitude A_{HF}; and
- modulation width ω: phase interval around $\varphi(\bar{z})$ comprising 68% of the cumulative high-frequency amplitude.

These steps are graphically depicted in Figs. S2–S4 by using synthetic data s(t). These data were constructed by superposing a sine wave of low frequency ($f_1 = 5$ Hz) and amplitude 1 with a sine wave of high frequency ($f_2 = 101$ Hz). The amplitude of the high-frequency sine wave was designed to vary between 0.05 and 0.25 depending on the phase of the low-frequency sine wave, such that the maximum amplitude was reached at the trough and the minimum amplitude was reached at the peak of the low-frequency wave.

$$A_1 = 1; f_1 = 5\ \text{Hz}$$

$$s_1(t) = A_1 \cdot e^{i \cdot 2\pi \cdot f_1 \cdot t}$$

$$A_2(t) = 0.1 \cdot (1.5 \cdot A_1 - \text{Re}(s(t))); f_2 = 101\text{Hz}$$

$$s_2(t) = A_2(t) \cdot e^{i \cdot 2\pi \cdot f_2 \cdot t}$$

$$s(t) = s_1(t) + s_2(t)$$

Furthermore, a noisy signal was constructed by adding a Gaussian distributed random variable with a mean of 0 and a standard deviation of 0.1 to s(t).

We compared results for the EEG signals with those for surrogate data, which exhibit the same power spectra as the original signals, but completely distorted phase characteristics (so-called scrambled data). To generate the scrambled data, EEG signals were transformed into the complex frequency domain by a fast Fourier transform (FFT). Then, the phases were randomized by adding a uniformly distributed random variable, which was uniformly distributed within the interval $[-\pi;\pi]$. Finally, the phase-randomized frequency values were back-transformed by FFT into the time domain.

Data were analyzed using the EEGLAG package created by A. Delorme and S. Makeig (4) running with MATLAB (The Mathworks), as well as by our own MATLAB programs. *P* values in the ANOVAs were Huynh-Feldt-corrected for inhomogeneities of covariance when necessary (5). Load effects were calculated using a linear parametric regression analysis with the number of maintained items (1, 2, and 4) as regressor.

The analysis of cross-frequency coupling across individual theta cycles during the maintenance phase (Fig. 1*G* and Fig. S6) was calculated as follows. First, zero-tapered demeaned data were wavelet-transformed in a range between 1 and 50 Hz using a five-cycle morlet wavelet, and power and phase values were calculated across time. Second, the peaks of theta (7 Hz) cycles were detected (zero crossings

from positive to negative values of the derivative of the time series filtered at 7 Hz). This resulted in an average of $7 \times 3.5 = 24.5$ theta cycles. Due to slight fluctuations of theta frequency and deviation from sine oscillations, some trials contained fewer than 24 cycles, but all trials had at least 20 theta cycles. Therefore, power values between 1 and 50 Hz were averaged (across all trials in each subject and then across all subjects) for the first 20 theta cycles. Next, power values between 1 and 50 Hz during 150 ms (slightly more than one theta cycle) centered around these time points were extracted. For each cycle and each frequency, power values were normalized by dividing by the average power across the respective cycle. The resulting values are depicted in Fig. 1*G*. Statistics are based on Rayleigh's test of nonuniformity (6). In detail, for each theta cycle, circular variance was quantified by transforming the distributions of beta/gamma power at 28 Hz (as depicted in Fig. S6) into complex vectors. This was done by constructing complex vectors given by the average gamma power (across patients) in each phase bin n, $\bar{\gamma}_n$, multiplied with $e^{i \cdot \varphi bin_n}$, where φbin_n denotes the average phase of each bin, and by averaging across these complex vectors. The angle of the resulting modulation vector indicates the center of the distribution of power values across phases. The length or absolute value of the vector quantifies the variance of the constructed complex vectors (7). The resulting value was compared with surrogate data obtained by permuting the values in the empirical distributions and computing surrogate modulation vectors; 1000 permutations were run for each cycle. *P* values were obtained by calculating the rank at which the sorted lengths of surrogate modulation vectors were superior to the empirical modulation vector (e.g., if the length of the empirical modulation vector was x, and 20 out of the 1000 surrogate modulation vectors had a length higher than x, the resulting *P* value was $20/1000 = 0.02$).

Analysis of Power and Phase Locking. EEG responses were filtered in the frequency range from 1 Hz to 200 Hz (1-Hz steps) by continuous wavelet transforms implementing Morlet wavelets with a bandwidth parameter $f_0/\sigma_f = 5$, that is, roughly speaking wavelets of five-cycle length (e.g., ref. 8). The complex filtered signals $w_{j,k}$ (j: time point within a trial, k: trial number) hereby result from the time convolution of original signals and the complex wavelet function. To avoid edge effects, EEG responses were segmented from −1000 ms to 4000 ms with respect to stimulus onset and, after wavelet transform, 500 ms at both sides were discarded. Based on the wavelet-transformed signals $w_{j,k}$, the phases $\varphi_{j,k}$ ($\varphi_{j,k} = \arctan(Im(w_{j,k})/Re(w_{j,k}))$) and the power values $P_{j,k}$ ($P_{j,k} = Re(w_{j,k})^2 + Im(w_{j,k})^2$) were extracted for each time point j of each trial k.

The calculation of intertrial phase-locking values was done by a procedure suitable for the evaluation of small and unequal trial numbers (e.g., ref. 9). Distributions of phases across trials were calculated separately for the different conditions (baseline, load 1, load 2, load 4, all trials). For this purpose, the phase domain was divided into 8 boxes of 45° covering the range from −180° to +180°. Distribution probabilities X_i were calculated for each box i and each time point j. Phase-locking values PL_j were then evaluated based on a normalized entropy measure: $PL_j = 1 + \sum_{i=1}^{8} X_{i,j} * \log X_{i,j}/\log(8)$. A large phase-locking or synchronization value indicates that phases or phase differences are not uniformly distributed but exhibit phase accumulations. To allow for a finer phase resolution, calculations were iterated for 45 shifts of the boxes about 1°. The phase-locking values result from the averages of these iterations.

Power and phase-locking values were averaged for nonoverlapping successive time windows of 100-ms duration from −500 to 3500 ms with respect to the onset of the last stimulus in each trial (40 windows in total). Afterward, values corresponding to the different time windows were divided by the prestimulus time range from −500 to 0 ms of the baseline condition separately for each subject and each filter frequency. We chose the prestimulus interval of the baseline condition for normalization so that the variation of normalized power and phase locking during baseline and maintenance intervals could be directly compared.

Results

If cross-frequency coupling were only due to event-related activity changes, it should be largely reduced during the second half of the maintenance phase as compared to the first half. We thus recalculated phase-power modulation during two consecutive nonoverlapping periods of 1750-ms length. The results are shown in Fig. S5 *D* and *E*. We found that modulation values during the two periods were 0.041 ± 0.010 in the first half and 0.043 ± 0.009 in the second half (mean ± SEM). Importantly, the modulation value in the second range, where no event-related activity occurs, is not significantly different from the value in the first range (the mean is even higher), indicating that modulation is not only due to event-related activity.

To exclude that these results were related to the shorter duration of the late maintenance phase as compared to the entire range, we also calculated cross-frequency coupling during the second half of the baseline period during the intertrial interval. Again, modulation was significantly enhanced during the second half of the maintenance phase as compared to the second half of the baseline period ($t_{13} = 5.74$; $p_{corr} < 0.001$).

Discussion

An association between hippocampal theta and gamma frequencies was also observed in awake behaving rats (10) (Fig. 2), although the frequency ratio was about twice as high as in our study. The frequency of hippocampal gamma band activity depends on the excitatory drive to interneurons as well as on the decay time constant of inhibitory postsynaptic currents, which can be enhanced by benzodiazepines (11). Hippocampal theta oscillations are generated by at least two distinct mechanisms (12). First, inputs from layers 2 and 3 of the entorhinal cortex are responsible for theta activity that persists after blockade of muscarinergic acetylcholine receptors. Second, due to tonic cholinergic excitation and phasic GABAergic inhibition of hippocampal interneurons by inputs from the medial band of broca and the septum, these interneurons induce rhythmic inhibitory postsynaptic potential (IPSPs) in the theta frequency range on their target pyramidal cells (in addition, it should be pointed out that the associational CA3 network has been proposed to function as an intrahippocampal theta generator, and that neurons within both the entorhinal cortex and hippocampus possess resonant properties in the theta frequency range). To our knowledge, it is unknown how an endogenous mechanism could simultaneously control the frequency of theta and gamma oscillations.

1. Van Roost D, Solymosi L, Schramm J, van Oosterwyck B, Elger C-E (1998) Depth electrode implantation in the length axis of the hippocampus for the presurgical evaluation of medial temporal lobe epilepsy: A computed tomography-based stereotactic insertion technique and its accuracy. *Neurosurgery* 43:819–826,discussion 826–827.
2. Axmacher N, et al. (2007) Sustained neural activity patterns during working memory in the human medial temporal lobe. *J Neurosci* 27:7807–7816.
3. Daubechies I (1990) The wavelet transform, time-frequency localization and signal analysis. *IEEE Trans Inf Theory* 36:961–1005.
4. Delorme A, Makeig S (2004) EEGLAB: An open source toolbox for analysis of single-trial EEG dynamics including independent component analysis. *J Neurosci Methods* 134:9–21.
5. Huynh H, Feldt LS (1976) Estimation of the box correction for degrees of freedom from sample data in the randomized plot and split plot designs. *J Educ Stat* 1:69–82.
6. Mardia K-V (1972) *Probability and Mathematical Statistics: Statistics of Directional Data* (Academic, London).
7. Canolty R-T, et al. (2006) High gamma power is phase-locked to theta oscillations in human neocortex. *Science* 313:1626–1628.
8. Lachaux J-P, Rodriguez E, Martinerie J, Varela F-J (1999) Measuring phase synchrony in brain signals. *Hum Brain Mapp* 8:194–208.
9. Fell J, et al. (2004) Neural bases of cognitive ERPs: More than phase reset. *J Cogn Neurosci* 16:1595–1604.
10. Bragin A, et al. (1995) Gamma (40–100 Hz) oscillation in the hippocampus of the behaving rat. *J Neurosci* 15:47–60.
11. Whittington M-A, Traub R-D, Jefferys J-G (1995) Synchronized oscillations in interneuron networks driven by metabotropic glutamate receptor activation. *Nature* 373:612–615.
12. Buzsáki G (2002) Theta oscillations in the hippocampus. *Neuron* 33:325–340.

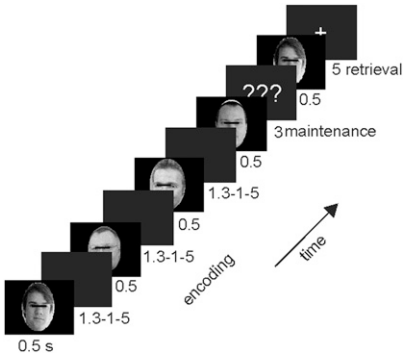

Fig. S1. Paradigm. We used a Sternberg paradigm with consecutive presentation of items (modified from ref. 2). Time is indicated in s. In different trials, either a single, two, or four trial-unique male or female faces with neutral emotional expression were presented.

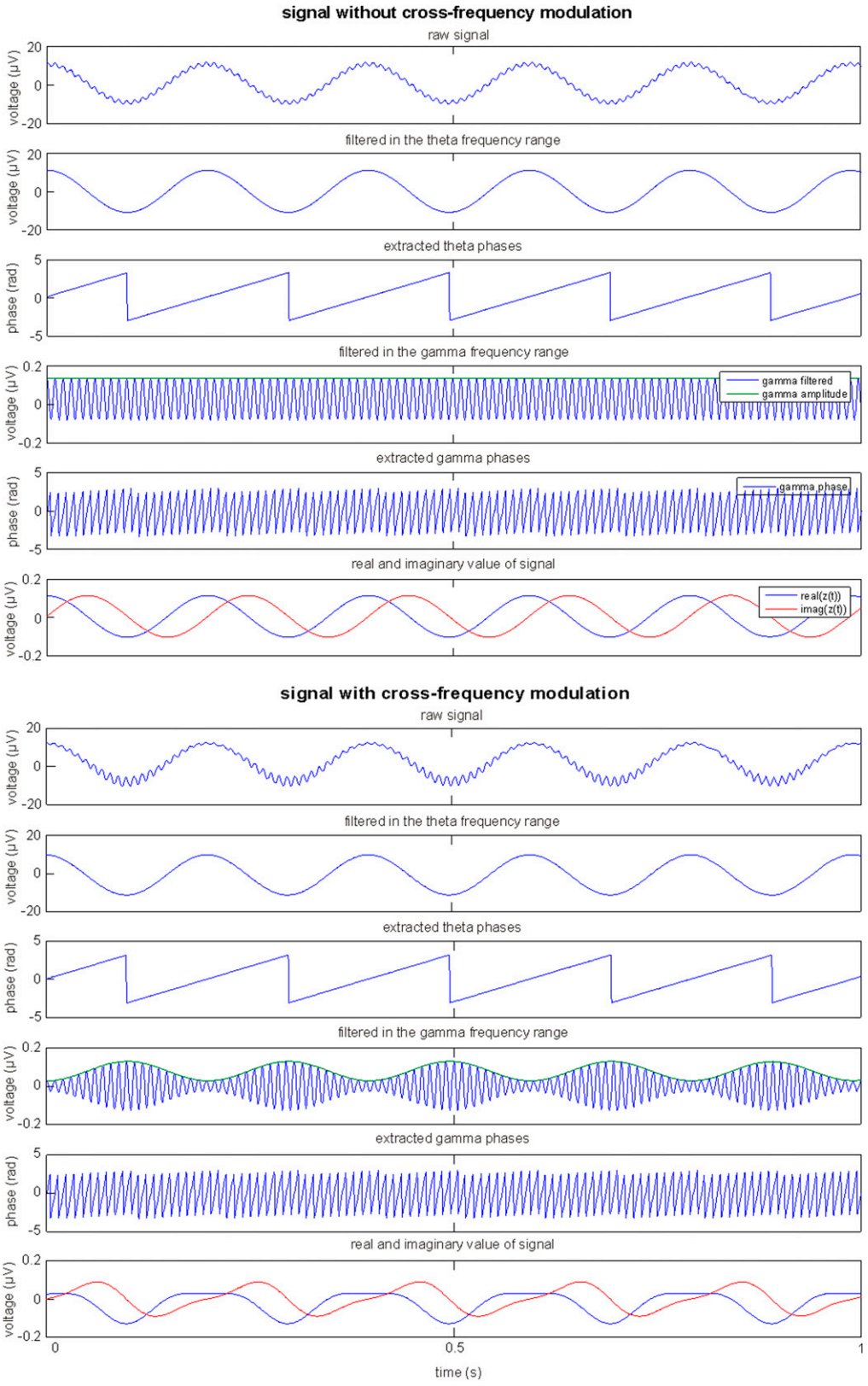

Fig. S2. Signal analysis part 1. Synthetic data without additional Gaussian noise.

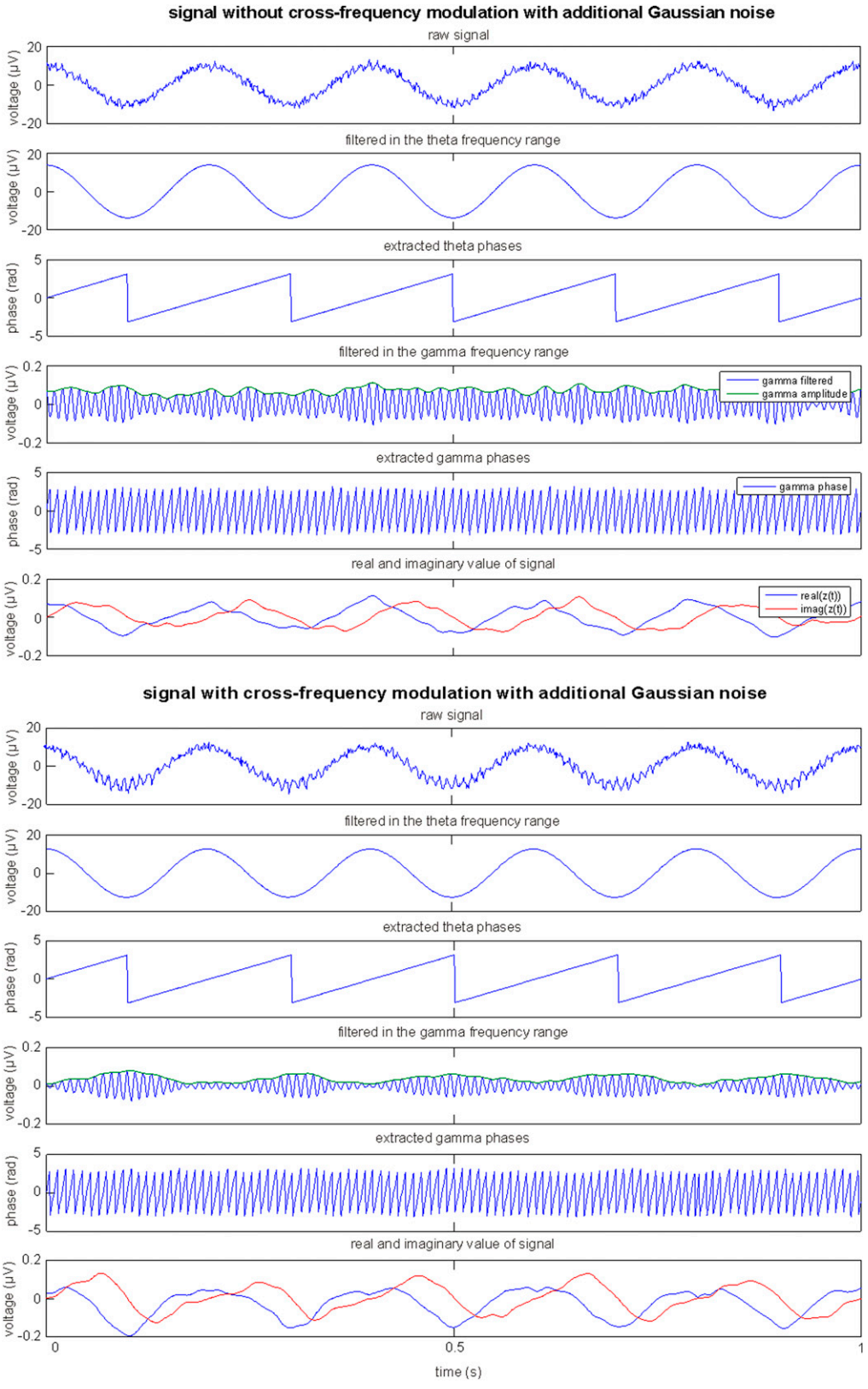

Fig. S3. Signal analysis part 2. Synthetic data with additional Gaussian noise.

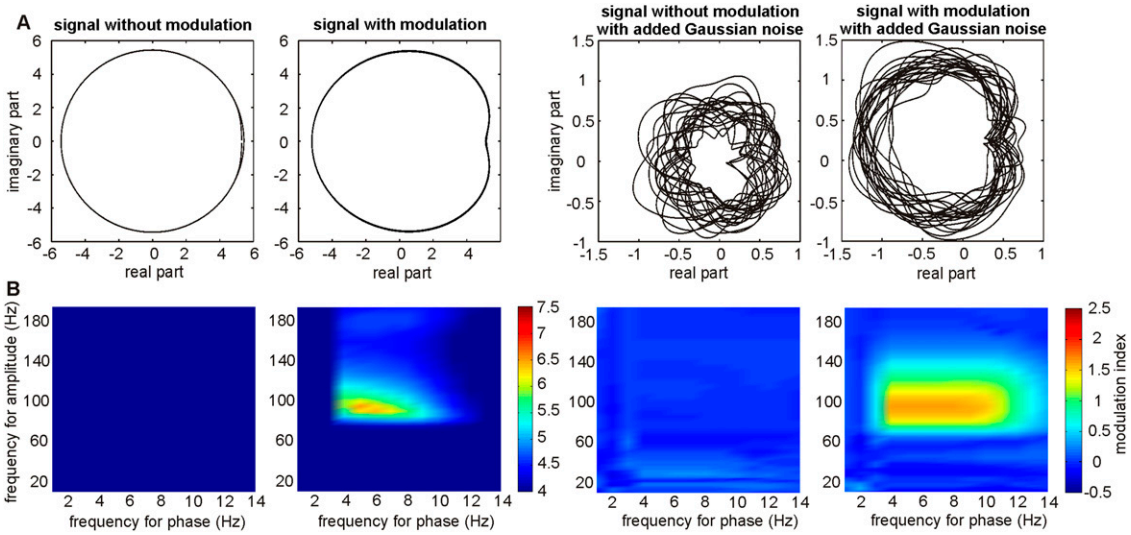

Fig. S4. Signal analysis part 3. (*A*) Modulation orbits for four different signal conditions (synthetic data). All plots depict complex modulation vectors given by $A_{HF}\, e^{i\Psi_{LF}}$ for consecutive time points across an interval of 3.5 s (where A_{HF} indicates high-frequency amplitude and Ψ_{LF} indicates low-frequency phase). Figures illustrate the time course of modulation vectors under realistic assumptions, that is, a phase-modulating low frequency in the theta range during a time interval of 3.5 s. (*B*) Cross-frequency coupling for four different signal conditions (synthetic data).

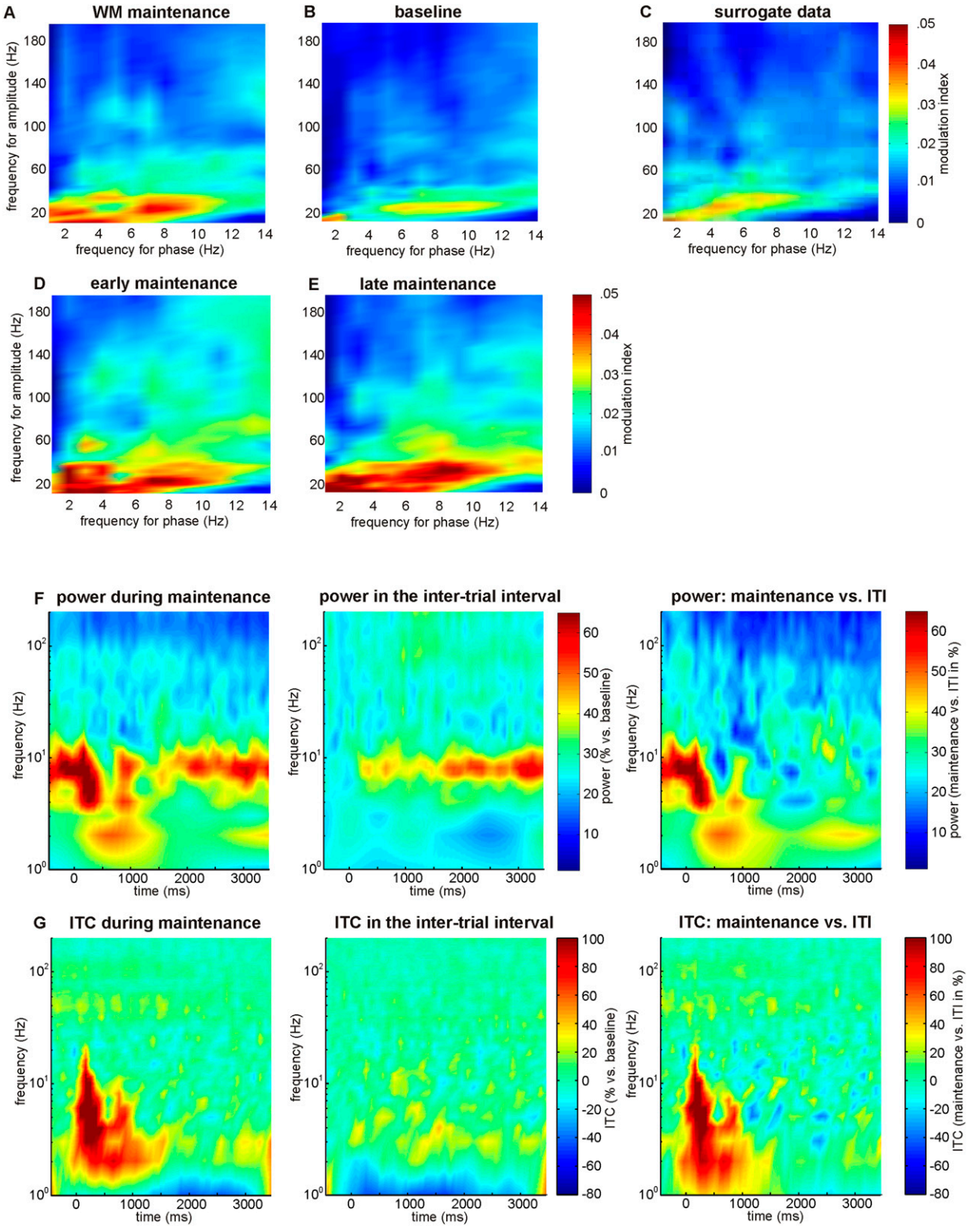

Fig. S5. Cross-frequency coupling does not depend on event-related changes of power and intertrial coherence. (*A*–*C*) Cross-frequency coupling in the entire frequency range between 1–14 Hz and 14–200 Hz during the maintenance phase (*A*), the baseline period in the intertrial interval (*B*), and the scrambled surrogate data (*C*). (*D* and *E*) Cross-frequency coupling during the first and second halves of the maintenance phase. Cross-frequency coupling in the early (0–1750 ms with respect to presentation of the last stimulus in each trial; *D*) and late (1750–3500 ms; *E*) maintenance phase were similar to, and quantitatively even more pronounced than, effects in the entire period. (*F* and *G*) Event-related spectral perturbations and intertrial coherence during maintenance as compared to the intertrial interval. (*F*) Analysis of event-related spectral perturbations shows sustained increases in the upper theta/lower alpha frequency range during the maintenance period and the intertrial interval (ITI). The direct comparison (right column) reveals only transient but no persistent differences between these two periods. Interestingly, there was already a preparatory theta power increase during the intertrial interval. (*G*) Intertrial phase coherence (ITC) was transiently increased between 1 and 20 Hz; no significant ITC was observed during the second phase of the maintenance period.

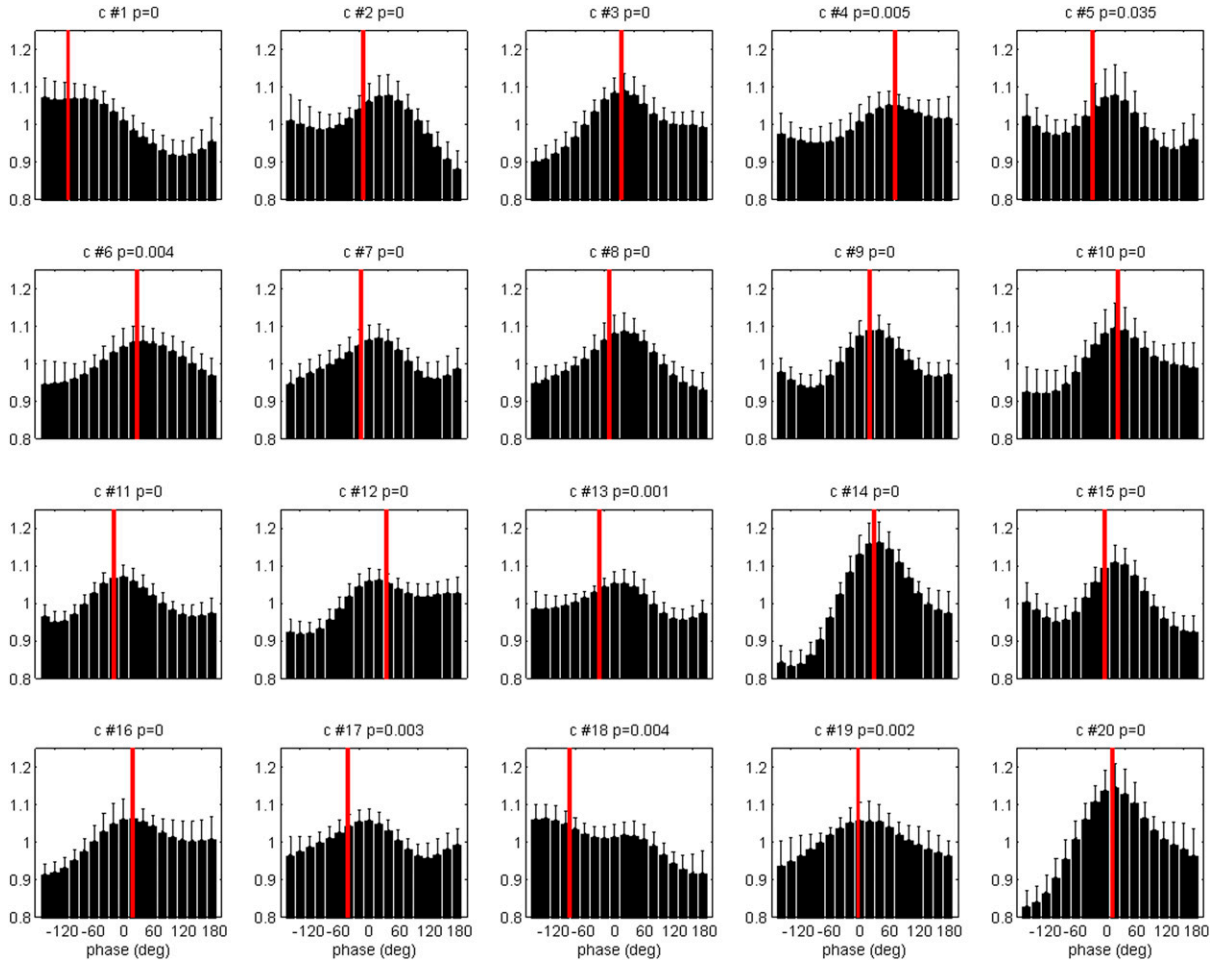

Fig. S6. Distributions of gamma power (at 28 Hz) across theta phase for the consecutive theta cycles during the maintenance period. For each cycle, the distribution depicts gamma power averaged across trials and patients together with standard errors of the mean. *P* values result from Rayleigh tests of nonuniformity as compared to surrogate data. Vertical red lines represent average phases of the modulation vectors. c #, cycle #.

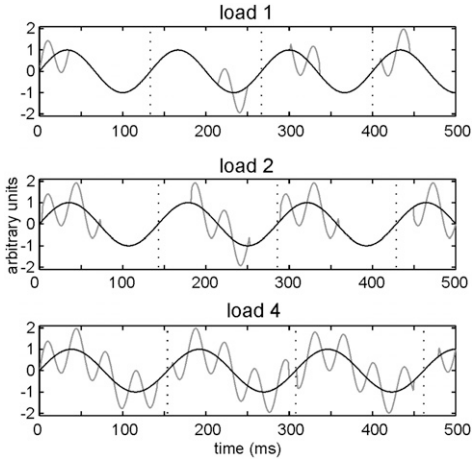

Fig. S7. Schematic overview of cross-frequency coupling in the different load conditions. This schematic depiction integrates the main finding on hippocampal cross-frequency coupling in the different working memory load conditions: The decreased modulating frequency (from 7.5 Hz in the load 1 condition to 6.5 Hz in the load 4 condition), a constant beta/gamma frequency (at 28 Hz), a decreased intertrial variance, and a constant modulation width (across all trials in one condition).

Table S1. MNI coordinates of selected electrode contact in each patient

x	y	z
24	−36	−1
−30	−12	−15
−16	−6	−24
−32	−33	−7
−28	−15	−17
29	−25	−11
33	−21	−14
−32	−27	−12
−30	−19	−16
−28	−7	−23
−21	−7	−25
33	−17	−15
30	−13	−18
32	−17	−14

Table S2. Individual maxima of modulation frequencies (in Hz)

Low frequency			High frequency		
Load 1	Load 2	Load 4	Load 1	Load 2	Load 4
7	7	6	22	16	16
9	7	6	28	42	22
6	6	6	16	28	26
7	6	6	16	38	20
6	10	7	14	46	30
7	7	6	26	16	28
6	7	6	44	20	16
8	8	8	30	32	28
6	6	7	36	16	38
7	7	8	28	26	50
10	6	6	50	38	24
7	10	6	42	34	22
10	6	6	46	18	16
9	7	6	26	28	14